Optics & Laser Technology, Volume 134, February 2021, Article number 106668
DOI:10.1016/j.optlastec.2020.106668

Inhomogeneous microstructure and fatigue crack propagation of thick-section high strength steel joint welded using double-sided hybrid fiber laser-arc welding

Jiecai Feng[ab]*, Liqun Li[a], Yanbin Chen[a]*, Yingzhong Tian[b], Yongle Sun[c], Xuanjun Zhang[d], Jie Zhang[d]

[a] State Key Laboratory of Advanced Welding and Joining, Harbin Institute of Technology, Harbin, 150001, P.R. China

[b] School of Mechatronic Engineering and Automation, Shanghai University, Shanghai 200444, P.R. China

[c] Welding Engineering and Laser Processing Centre, School of Aerospace, Transport and Manufacturing, Cranfield University, Cranfield, MK43 0AL, UK

[d] Shanghai Institute of Laser Technology, Shanghai 200233, P.R. China

* **Corresponding author at:** 99 Shangda Road BaoShan District, Shanghai 20444, P.R. China. Tel.: +86 021 56331820; Fax: +86 021 66743200. E-mail: fengjiecai@shu.edu.cn (Jiecai Feng), and 92 Xidazhi Street, Nangang District, Harbin City, Heilongjiang Province 150001, P.R. China. Tel.: +86 0451 86418645; fax: +86 0451 86415374. E-mail address: chenyb@hit.edu.cn (Yanbin Chen).

Abstract: The inhomogeneous microstructure and fatigue crack propagation of 30 mm thick-section high strength steel welded joint by double-sided hybrid fiber laser-arc welding were investigated in detail. The results indicated that the average effective grain size of the laser zone was only 1/2 of that of the arc zone, due to the

faster cooling rate of the laser resource. The base metal consisted of massive polygonal ferrites and small granular carbides, while weld metal were all composed of martensite with a high dislocation density. Compared with the arc zone, the percentage of grain boundaries with high misorientation angle increased 24% for the laser zone, as the average grain size of the laser zone was smaller than that of the arc zone. The results also revealed that the fatigue crack propagation resistance of the welded joint was higher than that of the base metal. Meanwhile, a significant increase in the fatigue crack propagation resistance of the laser zone occurred, as compared with the arc zone, due to the refined grains and the high proportion of the grain boundaries with high misorientation angle (>15°) in the laser zone.

Keywords: Welding; steel; microstructure; fatigue; fracture

1. Introduction

Hitherto, the thick-section high strength steels components are widely used in industries such as shipbuilding [1, 2], wind power tower [3], ocean engineering structures [4] and so on, due to their high strength, ductility and crack resistance. Shielded metal arc welding (SMAW), gas metal arc welding (GMAW), submerged arc welding (SAW) and gas tungsten arc welding (GTAW) are the commonly used welding techniques for the thick-section high strength steels [5, 6]. However, the efficiency of these arc welding process is very low because of their low penetration. Recently, hybrid laser-arc welding (HLAW), which has high penetration and is efficient and tolerant to gap, has been developed for joining the thick-section high strength steels [7-9].

In order to verify the long service reliability of the HLAW joints, their fatigue properties must be investigated, since most of the mechanical failure in high strength steel welded components arises from fatigue [10, 11]. In general, the fatigue fracture process can be divided into four stages: crack initiation, microscopic crack propagation (first stage propagation), macroscopic crack propagation (second stage propagation) and instantaneous fracture, according to the microscopic characteristics associated with the cracking from crack nucleation to fracture [12]. The fatigue crack propagation behavior could be affected by the microstructures (e.g. microconstituents, grain size and grain boundary angles) and mechanical properties (e.g. strength) of the welded joint [13-15]. Moeini et al. [16] reported that the non-isothermal conditions during laser welding resulted in a wide variety of microstructures, which strongly affected the fatigue properties of the welded joint. Dourado et al. [17] showed that the high strength steel joint made by laser welding showed better fatigue behavior when compared to that of arc welding. Kim and Hwang [18] also studied the fatigue properties of high strength steel laser and arc welded joints, and they found that the fatigue lives of the laser welded joint were approximately two times higher than those of the arc welded joint. Their study indicated that fatigue resistance can be attributed to the grain boundaries, which function as sources and sinks for the dislocations, and thus the finer grain size of the laser welded joint led to better fatigue properties, as compared to the arc welded joint. Hoshide et al. [19] and Marx et al. [20] also reported that fine grain size suppressed fatigue crack growth, since the grain boundaries were barriers suppressing the crack propagation. Therefore, for HLAW, it

is important to investigate the individual contributions of the laser zone and the arc zone to the fatigue crack propagation resistance of the HLAW joint.

In previous research, a novel double-sided hybrid laser-arc welding (DSHW) procedure has been designed to explore the benefits from the advantages of HLAW [21, 22]. The previous studies were focused on the mechanical properties, including the tensile strength and the impact toughness, as well as the microsturctures, such as the morphology and crystallography of the lath martensite in the weld metal. The purpose of this study is to elucidate the fatigue crack propagation of the thick-section high strength steel joint welded by DSHW, as well as fatigue properties of the individual parts including the laser zone, arc zone and base metal. The microstructures were characterized and the influence factors on the fatigue crack propagation of the inhomogeneous welded joint were analyzed.

2. Materials and methods

The materials used in this study were 30 mm thick high strength steel and filler wire, which are same as those used in previous studies by Chen et al. [21] and Feng et al. [22]. Their chemical compositions are listed in Table 1. A mixture of 95% Ar and 5% CO_2 with 25 l/min flow rate was used as shielding gas. The welding system consisted of two IPG fiber lasers (maximum powers are 5 kW and 10 kW) with wavelength of 1.07 μm and focus point diameter of 0.27 mm, offering two Fronius welding power options (maximum current is 400 A). The microstructure and fatigue crack propagation analyses were performed using the welded joints that were fabricated by four-pass DSHW process with optimized welding parameters. In the

first welding pass, the laser power, arc current and welding velocity were 4.7 kW, 200 A and 600 mm/min, respectively. In the second to fourth passes, the laser power, arc current and welding velocity were 1.9 kW, 218 A to 238 A and 800 mm/min, respectively. Details of the welding experiments can found in Refs. [21].

Table 1 Chemical composition of high strength steel and filler wire (wt.%).

	C	Mn	Ni	Cr	Mo	Si	P	S
Steel	0.11	0.57	4.47	0.60	0.40	0.25	0.010	0.008
Wire	0.05	1.72	2.50	0.60	0.60	0.40	0.009	0.009

The metallurgical specimens were etched by a solution of 5 ml nitric acid and 95 ml ethanol, and were observed using an OLYMPUS GX71 optical microscope. The fatigue fracture surface observation and crystallographic feature analysis were conducted using Quanta-200F and HELIOS NanoLab 600i models scanning electron microscopy (SEM) equipped with an electron backscattered diffraction (EBSD) system. The EBSD detection were operated at 30 kV with the specimen tilted by 70° and the scanning step was 0.8 μm. The transmission electron microscopy (TEM) observations were carried using a Tecnai G2 F30 microscope operated at 300 kV.

Low-cycle tensile-compressive fatigue crack propagation tests of 30 mm thick welded joints were performed at room temperature using a MTS 2500 KN system. The low-cycle fatigue crack propagation resistance is particularly important for service performance of ships due to their experienced loading states and possessed structures. The size and notch characteristic of the fatigue specimens for the fatigue crack propagation are shown in Fig. 1. A notch with width and deep of 0.5mm and 0.8mm, respectively, was prepared in the weld to facilitate the fatigue crack

propagation inside the weld. Fatigue cycling was imposed at a cyclic frequency of 0.2 Hz with triangular waveform and at a cyclic strain ratio of -1. A strain control process was adopted and the strain was 0.6%. The low-cycle tensile-tensile fatigue crack propagation tests of the laser zone, arc zone and base metal using standard compact fatigue crack propagation specimens (CT) were performed at room temperature by a MTS 809 KN system (Fig. 2). Fatigue cycling was imposed at a cyclic frequency of 0.2 Hz with triangular waveform and at a cyclic stress ratio of 0.1. A stress control process was employed and the applied peak load was 24 kN.

One of the most widely accepted models for fatigue analysis is the Paris' law [23], which offers a correlation between the linear elastic fracture mechanics (LEFM) and the fatigue crack propagation. The Paris' law relates the fatigue crack propagation length (a) per cycle to the variation range (ΔK) of the stress intensity factor during cyclic loading [24-26]. Thus, the Paris' law is employed here to describe the fatigue crack propagation characteristic.

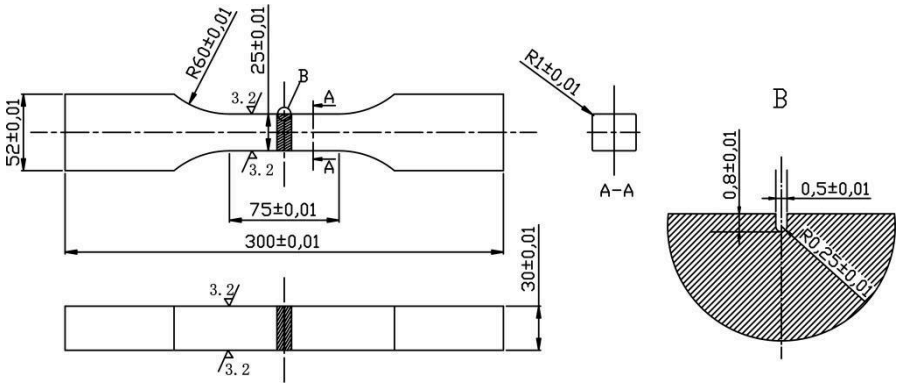

Fig. 1. Dimensions of fatigue specimen of welded joint.

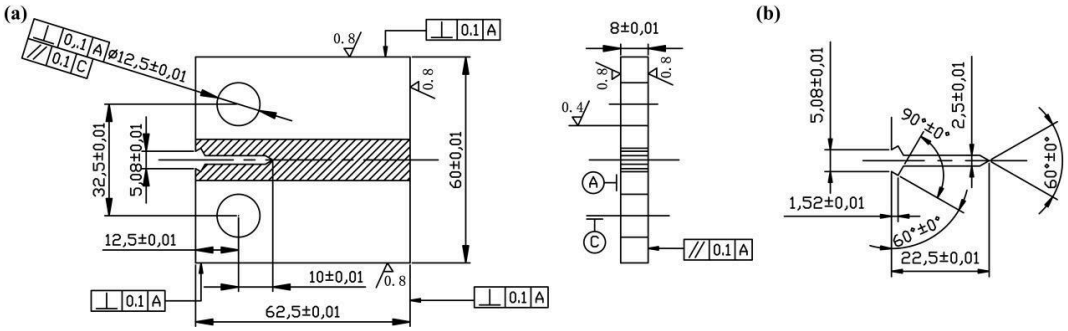

Fig. 2. Dimensions of: **(a)** CT fatigue specimen and **(b)** Notch in the CT fatigue specimen.

3. Results

3.1 Microstructure

The macrograph of the cross-section of the welded joint by DSHW is presented in Fig. 3. It is clearly seen that the welded joint is in a shape of dumbbell and a narrow deep zone was formed in the middle of the welded joint, which has the characteristics of the laser weld. On the contrary, two wide shallow zones with arc weld features are acquired on both sides of the welded joint. The microstructure and fatigue crack propagation would be different between the two zones. Therefore, for the purposes of later discussion, here the middle narrow deep zone and the bilateral wide shallow zone are named as laser zone and arc zone, respectively.

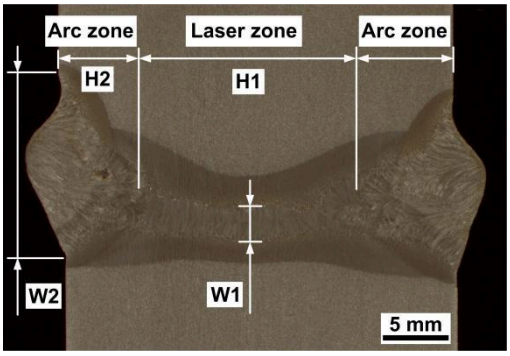

Fig. 3. Inhomogeneous dimension of joint welded using double-sided hybrid laser-arc welding.

It should be noted that, the penetration (H1) and the width (W1) of the laser zone are about 16.5 mm and 2.6 mm, respectively, indicating that the depth-width ratio is as high as 6.3. However, the penetration (H2) and the width (W2) of the arc zone are approximate 6.75 mm and 14.1 mm, respectively, resulting in a low depth-width ratio of 0.5. The average penetration of the laser zone is about 2 times of that of the arc zone, while the average width of the laser zone is only 1/4 of that of the arc zone.

The microstructure of the laser zone is shown in Fig. 4. The base metal consists of massive polygonal ferrites and small granular carbides (Fig. 4(b)). While, the HAZ is composed of partially transformed region (Fig. 4(c)), fine grained region (Fig. 4(d)) and coarse grained region (Fig. 4(e)). The fine grained region, the coarse grained region and weld metal (WM) are all composed of martensite.

Fig. 5 shows the similar microstructure of the arc zone. The HAZ is also composed of partially transformed region, fine grained region and coarse grained region (Fig. 5(b) and (c)). The fine grained region, the coarse grained region and weld metal also consist martensite microstructure (Fig. 5(d)-(f)).

The microstructures of BM, HAZ and WM of laser zone, as well as WM of arc zone were further examined by TEM, and their substructures are shown in Fig. 6. As shown in Fig. 6(a), in the ferrites of the BM, precipitation of granular carbides is observed, while, in the HAZ and WM of laser zone, and the WM of arc zone, lath martensites with a high dislocation density in the ferrite matrix are acquired (Fig. 6(b) to (d)).

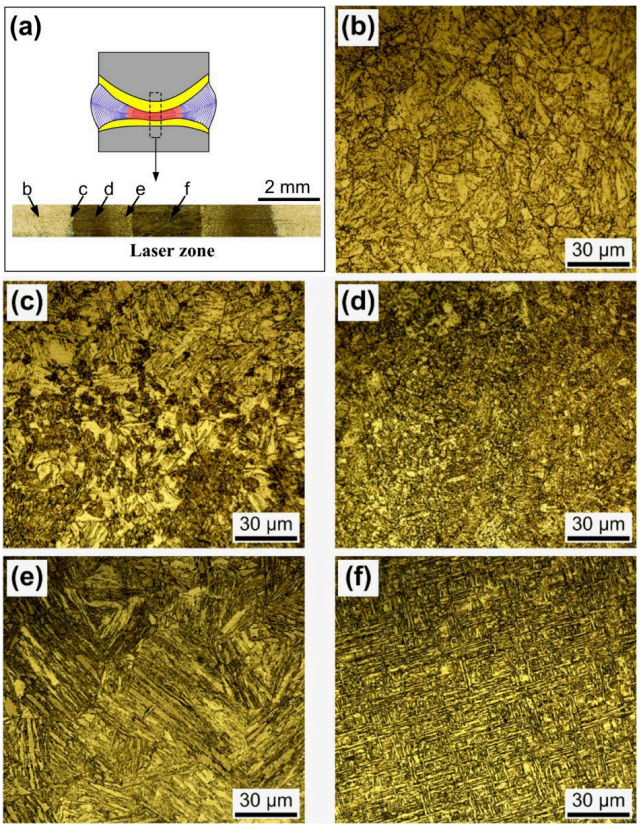

Fig. 4. Microstructure of laser zone: **(a)** Schematic diagram, **(b)** Base metal, **(c)** Partially transformed region, **(d)** Fine grained region, **(e)** Coarse grained region and **(f)** Weld metal.

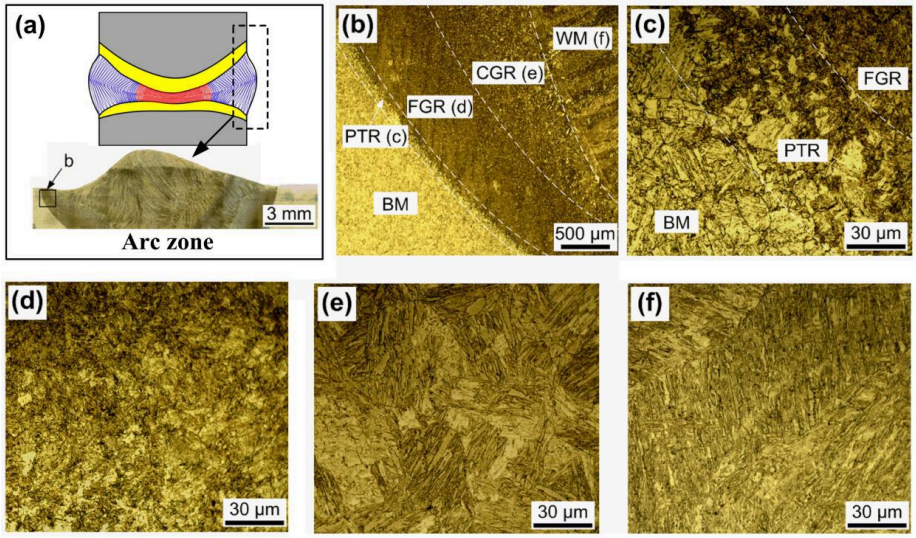

Fig. 5. Microstructure of arc zone: **(a)** Schematic diagram, **(b)** Different regions of weld, **(c)** Partially transformed region, **(d)** Fine grained region, **(e)** Coarse grained region and **(f)** Weld metal.

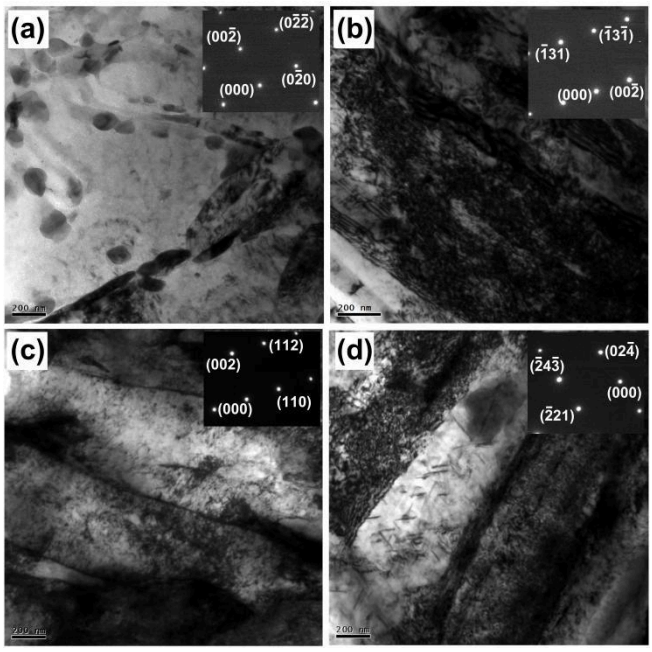

Fig. 6. TEM comparison of: **(a)** Base metal, **(b)** HAZ of laser zone, **(c)** WM of laser zone and **(d)** WM of arc zone.

In order to better understand the different fatigue crack propagation features of the base metal, laser zone and arc zone, the crystallographic characteristics of these zones were investigated using EBSD. Distribution diagrams of grain size and the inverse pole figure (IPF) with high misorientation grain boundary (>15°) are shown in Fig. 7, which reveals that the average effective grain size of the base metal is 15.8 μm, while those of the laser zone and arc zone are 4.2 μm and 8.1 μm, respectively. The average effective grain size of the arc zone is 1.9 times larger than that of the laser zone. Additionally, the average effective grain size of the base metal is 3.8 times and 2 times larger than those of the laser zone and arc zone, respectively. Such a difference arises because the laser zone was formed mainly due to the laser energy, while the arc zone was mainly determined by the arc heat source. The cooling rate of the laser welding is higher than that of the arc welding [27, 28]. Consequently, the grain

growth of the laser zone is restricted, as the grain growth time for the laser zone is shorter than that for the arc zone, resulting in smaller grain size in the laser zone.

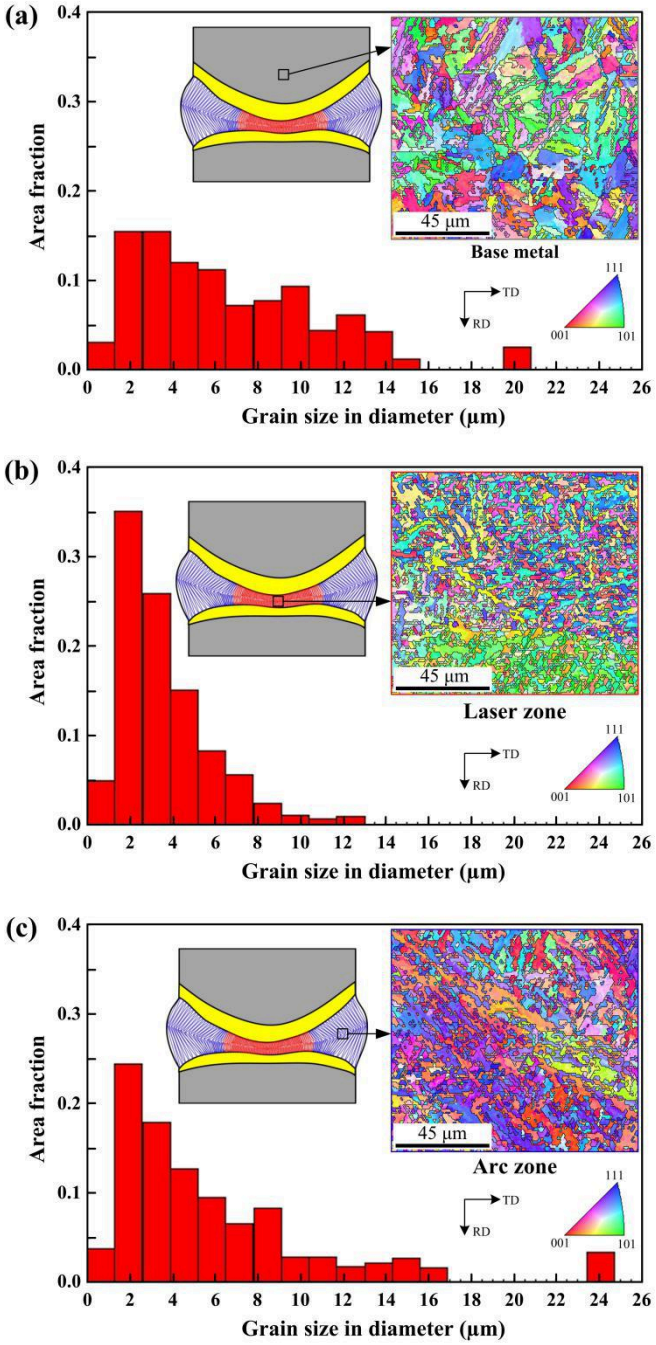

Fig. 7. Inverse pole figure (IPF) with high misorientation (>15°) grain boundary and grain size distribution of: **(a)** Base metal, **(b)** Laser zone and **(c)** Arc zone.

Fig. 8 shows the distribution diagrams of grain boundary angles in the base metal, laser zone and arc zone. The statistical analysis indicates that the percentages of the

grain boundaries with high misorientation angle (>15°) of the base metal, laser zone and arc zone are 50.5%, 64.2% and 51.8%, respectively. The percentage of grain boundaries with high misorientation angle of the laser zone increased 24% compared with that of the arc zone. This is because the grain size of the laser zone is smaller than that of the arc zone. Additionally, the previous experimental results show that the grain boundary angles of the laser zone and arc zone are both approximately 60° [21]. Consequently, the percentage of grain boundaries with high misorientation angle of the laser zone is larger than that of the arc zone.

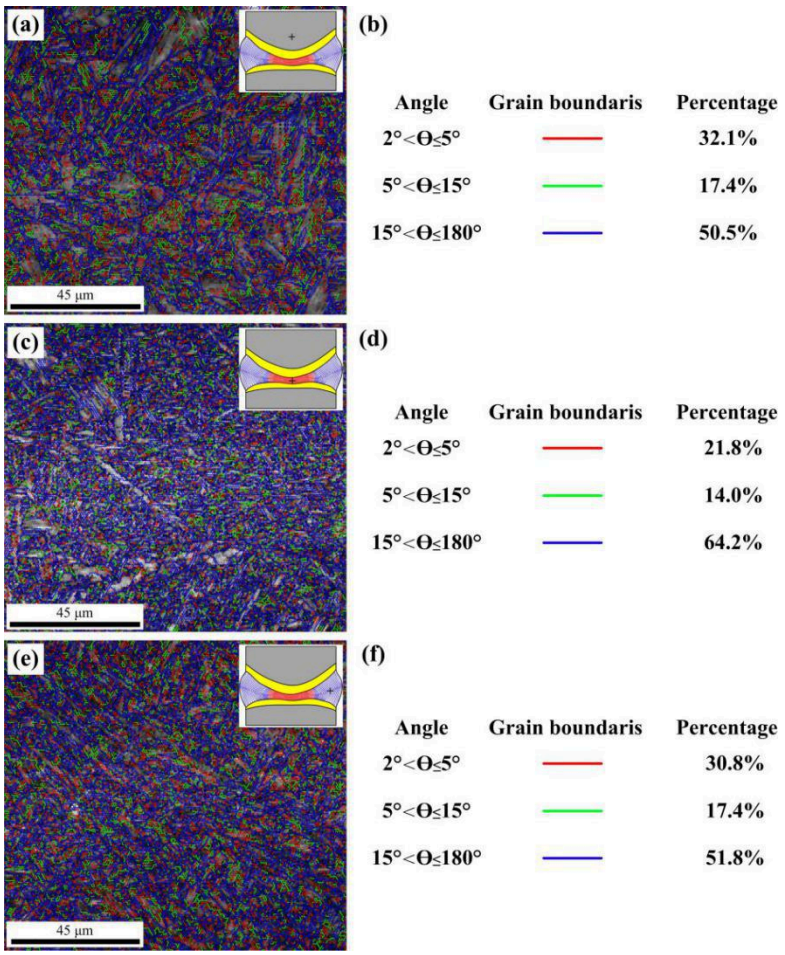

Fig. 8. The distribution diagrams and percentages of misorientation angle of grain boundaries: **(a)** Base metal, **(b)** Laser zone and **(c)** Arc zone.

3.2 Fatigue crack propagation of integral welded joint

The fatigue crack propagation path of the integral welded joint and the base metal are shown in Fig. 9(a) and (b), respectively. It is evident that the fatigue crack extended from the preset notch on the right-hand side of the welded joint when the tension-pressure load was applied and the fatigue crack propagation path of the welded joint is tortuous (Fig. 9(a)). Velu [29] also reported that fatigue cracks always deviate towards the materials of low strength, resulting in tortuous crack propagation path. However, the fatigue crack propagation path of the base metal is relatively straight (Fig. 9(b)) because of the uniform microstructure of the base metal.

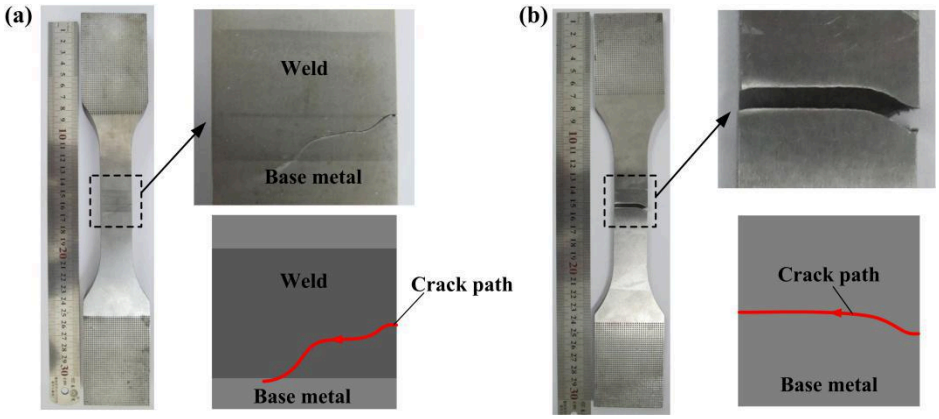

Fig. 9. Fatigue crack path of: **(a)** Welded joint and **(b)** Base metal.

The first stage of the fatigue crack propagation is very short, usually propagating less than 1 mm. On the contrary, the second stage of fatigue crack propagation is very long and almost accounts for the whole fatigue fracture process, which is a key stage to analyze the fatigue crack propagation. In general, the second stage of the fatigue crack propagation is divided into three regimes: low speed propagation regime, medium speed propagation regime and high speed propagation regime [30].

The fracture morphology of fatigue crack of the base metal and the welded joint at low speed propagation regime is presented in Fig. 10(a) and (b). It shows that tire indentation is observed in the fatigue crack propagation fractures of both the base material and the welded joint. This is because in the process of the fatigue crack propagation, the edges, particles or bumps on the two matching fracture surfaces jump forward under the cyclic loading, resulting in rows of indentations which are roughly parallel to each other. Tire indentation is a common microscopic feature of the low cycle fatigue fracture. Compared with tension-tension fatigue loading, tension-compression fatigue loading is more likely to produce tire indentation on the fracture surface. Forsyth and Ryder [31] indicated that tire indentation striation spacing represented the fatigue crack growth distance per fatigue cycle. Smaller striation space resulted in lower fatigue crack propagation rate, on the contrary, larger striation space leaded to faster fatigue crack propagation rate. Fig. 10(a) and (b) present that the space between the tire indentation for the fatigue fracture of the welded joint is smaller to that of the base material, indicating that the fatigue crack propagation rate of the welded joint is lower than that of the base metal.

The fatigue fracture morphology of the base metal and the welded joint in medium speed propagation regime is shown in Fig. 10(c) and (d), respectively. It is evident that compared with low speed propagation regime (Fig. 10(a) and (b)), the space between the tire indentation for the fatigue fracture of both the welded joint and the base metal at medium speed propagation is larger. Furthermore, it is observed that the space between the tire indentation for the fatigue fracture of the welded joint is

smaller than that for the base material, which indicates that the fatigue crack propagation rate of the welded joint is lower than that of the base metal.

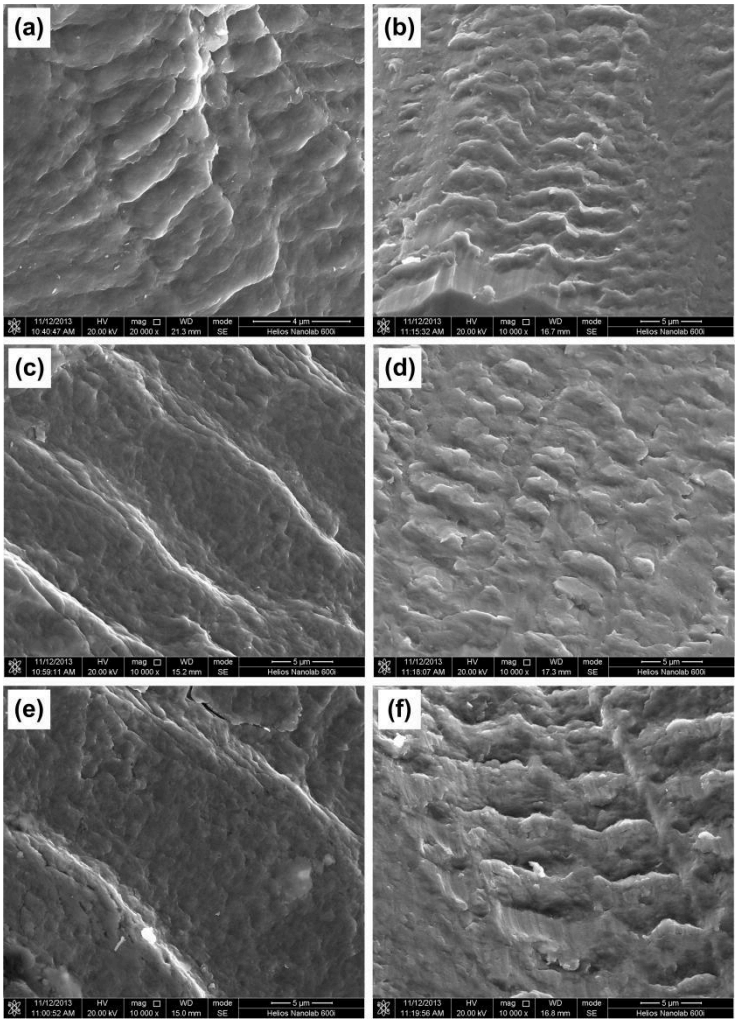

Fig. 10. Fatigue fracture morphology of: the low speed crack growth regime of **(a)** Base metal and **(b)** Integral welded joint, the medium speed crack growth regime of **(c)** Base metal and **(d)** Integral welded joint, the high speed crack growth regime of **(e)** Base metal and **(f)** Integral welded joint.

The fracture morphology of fatigue crack of the base metal and the welded joint in the high speed propagation zone is indicated in Fig. 10(e) and (f), respectively. It shows that compared with low and medium speed propagation zones (Fig. 10(a) to

(d)), the space between the tire indentation for the fatigue fracture of the welded joint and the base metal in the high speed propagation is the largest. Furthermore, the space between the tire indentation for the fatigue fracture of the welded joint is smaller than that for the base material, indicating, again, that the fatigue crack propagation rate of the welded joint is lower than that of the base metal, as shown in Fig. 10(e) and (f).

The fatigue fracture morphology of the base metal and the welded joint at the instantaneous fracture stage is shown in Fig. 11. Dimples are observed on the fatigue fracture surfaces of both the base metal and the welded joint, meaning that at the instantaneous fracture stage, the fracture patterns of the base metal and welded joint are similar to that of the ductile fracture under static load.

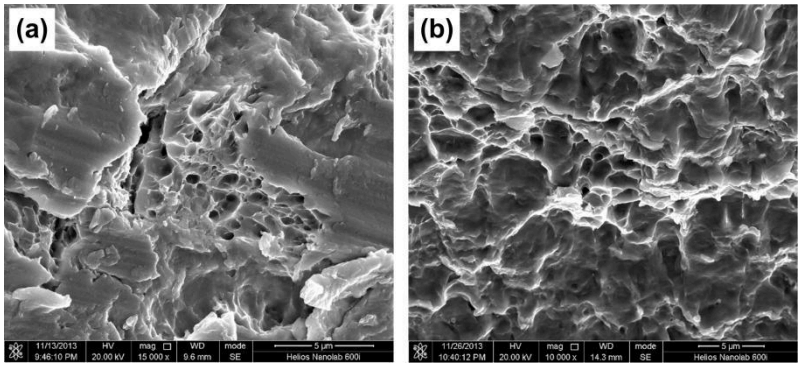

Fig. 11. Fatigue fracture morphology of instantaneous fracture regime of: **(a)** Base metal and **(b)** Integral welded joint.

3.3 Fatigue crack propagation of laser zone, arc zone and base metal

In order to analyze the individual contributions of the laser zone and the arc zone to the fatigue crack propagation resistance of the integral welded joint, the fatigue crack propagation rates and fracture morphologies of the base metal, laser zone and arc zone were investigated in details.

3.3.1 Fatigue crack propagation rate

The relationships between the fatigue crack length and the number of cycles for the base metal, laser zone and arc zone are shown in Fig. 12. The fatigue crack length of the laser zone is the shortest, followed by that of the arc zone, while the fatigue crack length of the base metal is the longest, for the same number of cycles. When the number of the cycles is 4000, the fatigue crack length of the laser zone is 13% and 16% shorter than that of the arc zone and base metal, respectively. Therefore, the fatigue resistance of the laser zone is higher than that of the arc zone, while the fatigue resistance of the base metal is the lowest.

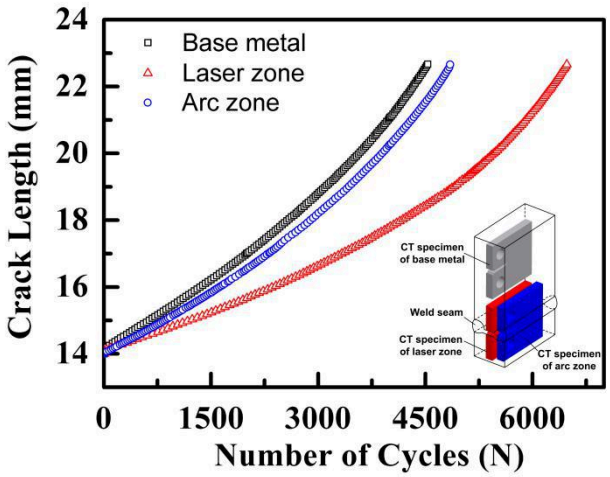

Fig. 12. Fatigue crack growth curves.

The double logarithm relationship between the fatigue crack propagation rate *da/dN* and the stress intensity factor range ΔK of the base metal, laser zone and arc zone is presented in Fig. 13. It is clearly seen that all the *da/dN* - ΔK curves for the base metal, laser zone and arc zone are approximately linear, satisfying the Pairs' law expressed in the double logarithm coordinate system.

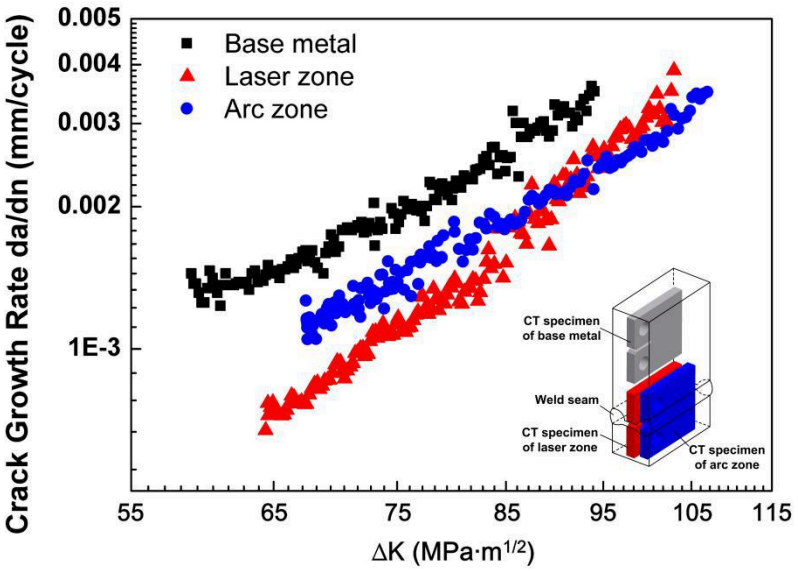

Fig. 13. Fatigue crack growth rate curves.

The propagation rate and mode of fatigue crack are mainly dependent on the microstructure and mechanical properties, when the extrinsic conditions such as the fatigue load, frequency and stress ratio are identical. The stress intensity factor range (ΔK) is the driving force for the fatigue crack growth, its increase results in higher values of the fatigue crack propagation rate (da/dN), as shown in Fig. 13. It should be noted that a notch was prefabricated in the compact fatigue crack growth specimen and consequently, stress concentration occurred near the notch, from where the fatigue crack would begin to propagate. At the first stage of the fatigue crack propagation, the local stress field at the crack tip is relatively high due to the fatigue cycle load. Consequently, the dislocation keeps moving, resulting in dense slip band at the crack tip. The depth and width of the slip band increase continuously and the fatigue microcrack is formed, with increase in the number of the loading cycles. The fatigue macrocrack occurs as a result of the increases in the length of the fatigue microcracks, indicating the second stage of the fatigue crack propagation. As the

fatigue crack propagates, the crack length increases further. Meanwhile, the stress concentration at the tip of the fatigue crack increases.

From Fig. 13 it is also evident that the fatigue crack propagation rates of both the laser zone and arc zone are lower than that of the base metal, which indicates that the fatigue crack propagation resistance of the laser zone and arc zone is higher than that of the base metal in the low speed, medium speed and high speed regimes for the fatigue crack propagation. This difference is consistent with the experimental observation of the tire indentation of the welded joint and the base metal, as shown in Fig. 10. It is interesting to see that the fatigue crack propagation rate of the laser zone is lower than that of the arc zone, when the stress intensity factor range is no greater than 95 $MPa \cdot m^{1/2}$. However, the fatigue crack propagation rate of the laser zone is higher than that of the arc zone when the stress intensity factor range exceeds 95 $MPa \cdot m^{1/2}$. Thus, the fatigue crack propagation resistance of the laser zone is larger than that of the arc zone in the low speed and medium speed regimes of the fatigue crack propagation. On the contrary, the fatigue crack propagation resistance of the laser zone is lower than that of the arc zone at the high speed regime of the fatigue crack propagation. This is probably because at the end of the fatigue test for the laser zone, the crack extends into the base metal as the average width of the laser zone is only 2.6 mm, resulting in high propagation rate of the fatigue crack. It is also evident that compared with the arc zone and the base metal, the fatigue crack propagation rate of the laser zone decreases by 17% and 37%, respectively, when the stress intensity factor range is 80 $MPa \cdot m^{1/2}$.

3.3.2 Fracture morphology of fatigue crack propagation

The fracture morphology of the macroscopic fatigue crack propagation (second stage propagation) of the base metal, laser zone and arc zone were investigated in detail.

The fatigue fracture morphology of the base metal, laser zone and arc zone at the low speed regime of the macroscopic fatigue crack propagation is presented in Fig. 14 (a) to (c). Fatigue bands are observed in the fracture morphology of all the base metal, laser zone and arc zone, indicating that the mechanisms of fatigue crack propagation of the base metal, laser zone and arc zone are plastic band propagation. During the fatigue crack propagation process, the crack tip expands and opens when the fatigue load is applied, while the crack tip blunts and closes at the unload stage. Thus, a fatigue band is formed during each tensile load cycle. In an ideal situation, each fatigue band represents the corresponding cyclic load, and the number of the fatigue bands is equal to the number of the load cycles.

The fatigue fracture morphology of the base metal, laser zone and arc zone in the medium speed regime of the macroscopic fatigue crack propagation is shown in Fig. 14(d) to (f). Compared with the low speed propagation regime, all the space of the fatigue bands of the base metal, laser zone and arc zone increases in the medium speed regime, respectively.

Fig. 14(g) to (i) indicate that compared with the medium speed propagation regime, all the space of the fatigue bands of the base metal, laser zone and arc zone

increases at the high speed regime, respectively. Consequently, the space of the fatigue band of the base metal, laser zone and arc zone increases, respectively, as the fatigue crack expands from the low speed regime to the medium speed regime, followed by the high speed regime.

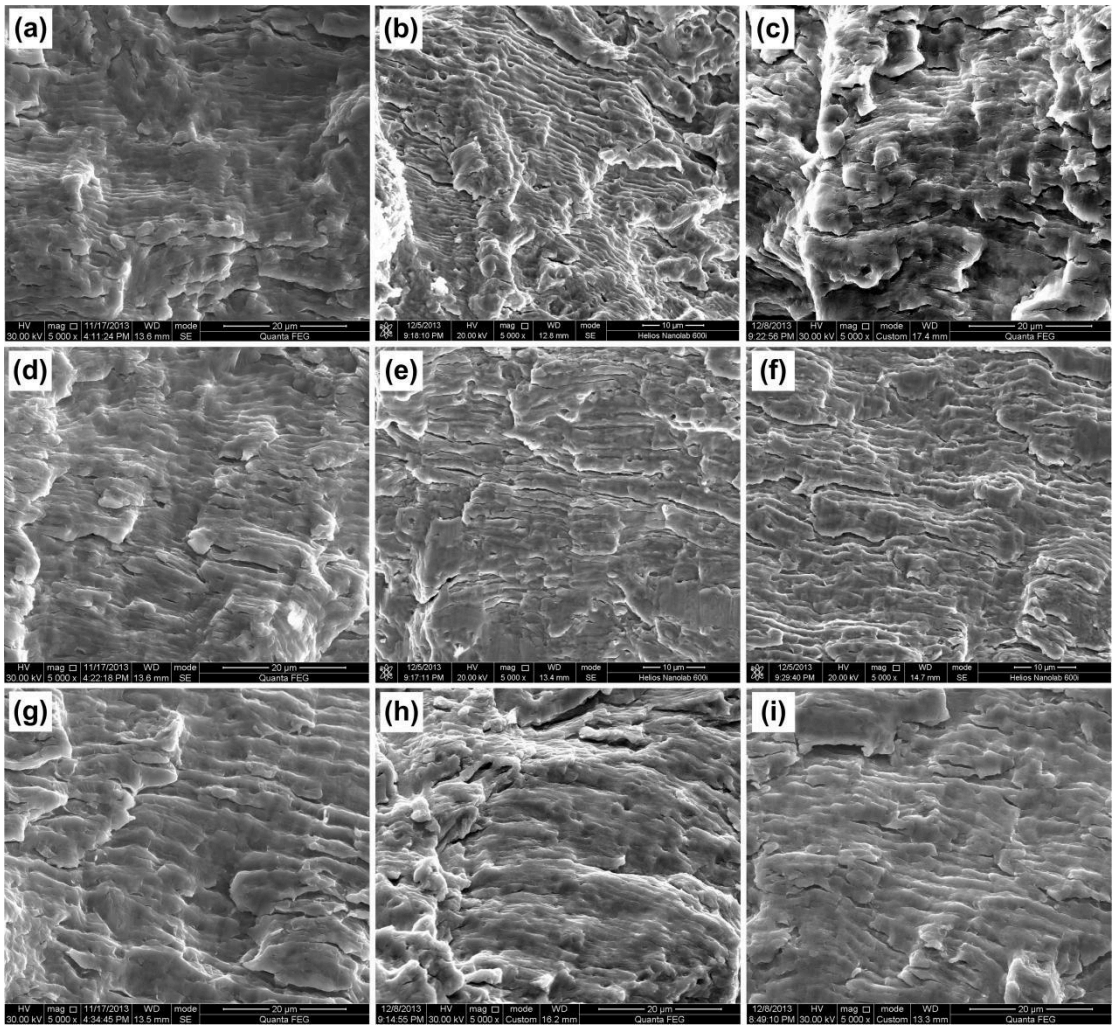

Fig. 14. Fatigue fracture morphology of CT specimens of: the low speed crack growth regime of **(a)** Base metal, **(b)** Laser zone and **(c)** Arc zone, the middle speed crack growth regime of **(d)** Base metal, **(e)** Laser zone and **(f)** Arc zone, the high speed crack growth regime of **(j)** Base metal, **(h)** Laser zone and **(i)** Arc zone.

It should be noted that the space of the fatigue band of the laser zone is smaller

than that of the arc zone, as shown in Fig. 14, which indicates that the fatigue crack propagation rate of the laser zone is lower than that of the arc zone. Additionally, the space of the fatigue band of both the laser zone and the arc zone is smaller than that of the base metal, which demonstrates that the fatigue crack propagation resistance of both the laser zone and the arc zone is higher than that of the base metal. The space of the fatigue band on the fatigue fracture of the base metal, laser zone and arc zone reflects the fatigue crack propagation rate, which is consistent with the measured fatigue crack growth rate curves (Fig. 13).

4. Discussion

The factors affecting fatigue crack propagation can be categorized as intrinsic factors and extrinsic factors. The intrinsic factors mainly include the microstructure and the properties, while the extrinsic factors are mainly manifested as the thickness of specimen, stress ratio, load frequency and so on. The effects of the intrinsic factors such as the yield strength, Young's modulus, microstructure and grain boundary angle on the fatigue crack propagation were investigated in detail, while the extrinsic factors were discussed accordingly.

4.1 Effect of yield strength on the fatigue crack propagation

The K_I represents the driving force of the fatigue crack propagation, which can be expressed as [32]:

$$K_I = Y\sigma\sqrt{\pi a} \tag{1}$$

where Y represents the coefficient of the fatigue crack shape, σ represents the stress

of the load and *a* represents the length of the fatigue crack.

In the actual process of the fatigue crack propagation, there is a small plastic deformation zone at the tip of the fatigue crack. Let *r* represent the radius of the small plastic deformation zone at the tip of the fatigue crack in the polar coordinates (*r, θ*), then the K_I can be modified as follows [32],

$$K_I = Y\sigma\sqrt{\pi(a + r_y)} \tag{2}$$

where r_y represents the projection of the radius (*r*) of the small plastic deformation zone at the tip of the fatigue crack onto the *y*-axis of the *x*-*y* coordinate system, which can be expressed as,

$$r_y = \frac{1}{4\sqrt{2}\pi}(\frac{K_I}{\sigma_S})^2 \tag{3}$$

where σ_s represents the yield strength of the materials.

The simultaneous equations (2) and (3),

$$\sqrt{\quad}\sqrt{\quad\frac{Y^2}{4\sqrt{2}}(\frac{\sigma}{\sigma_S}} \tag{4}$$

The larger the yield strength of the material, the smaller the modified principal stress intensity factor K_I, resulting in lower fatigue crack propagation rate, according to the Eq. (4).

It has been reported that the yield strength of the base metal, laser zone and arc zone were 831 MPa, 942 MPa and 893 MPa, respectively [21]. Thus, the modified principal stress intensity factor of the base metal is the maximum followed by that of the arc zone, while that of the laser zone is the minimum. Therefore, considering only the value of principal stress intensity factor, the driving force of the fatigue crack

propagation of the laser zone is the lowest, resulting in lowest fatigue crack propagation rate. Consequently, the fatigue crack propagation resistance of the laser zone is the maximum followed by that of the arc zone, while that of the base metal is the minimum. This is consistent with the measured fatigue crack growth rate curves (Fig. 13). It should be noted that, yield strength represents the ability of materials to resist plastic deformation, which is closely related to the microstructure and grain size of materials. Thus, the microstructure and the grain size of materials, as discussed later, are essential to the yield strength to affect the fatigue crack propagation resistance.

4.2 Effect of Young's modulus on the fatigue crack propagation

As the mechanism of the fatigue crack propagation of the base metal, laser zone and arc zone is plastic band expansion, the fatigue crack propagation rate is expressed as,

$$da / dN = C\Delta K_{eff}{}^{m} \tag{5}$$

$$C = \frac{1}{2\pi(0.1E)^2} \tag{6}$$

where the a represents the length of the fatigue crack, the N represents the number of the load cycles, C and m represent the parameters of the material and E represents the Young's modulus.

The fatigue crack propagation rate is inversely proportional to the square of the Young's modulus according to Eqs. (5) and (6). The Young's moduli of the base metal, laser zone and arc zone are $1.62\times10^5 MP$a , $1.84\times10^5 MP$a and $1.78\times10^5 MP$a , respectively, according to previous tensile test results [21]. The Young's modulus of

the laser zone is the maximum followed by the arc zone, while that of the base metal is the minimum. Therefore, the fatigue crack propagation resistance of the laser zone is the largest and that of the arc zone is in the middle, while that of the base metal is the lowest, which is consistent with the measured fatigue crack growth rate curves measured (Fig. 13).

The Young's modulus represents the bonding strength between atoms, ions or molecules. It is affected by the factors such as the chemical composition, crystal structure and microstructure of the material as well as the environmental temperature, which affect the fatigue crack propagation resistance.

4.3 Effect of microstructure on the fatigue crack propagation

The microstructure of the base metal is tempered sorbite, while that of the laser zone and arc zone are lath martensite due to the fast cooling rate of the hybrid laser-arc welding process. Compared with the tempered sorbite, the lath martensite containing high density dislocation is plastic deformed in the front of the fatigue crack tip [33, 34]. Therefore, the stress concentration in the front of the fatigue crack propagation is reduced to a certain extent due to the large plastic deformation in the front of the fatigue crack propagation. Thus, the driving force of the fatigue crack propagation decreases, thereby enhancing the fatigue crack propagation resistance [30]. Consequently, the fatigue crack propagation resistance of the laser zone and arc zone containing lath martensite is higher than that of the base metal.

4.4 Effect of grain boundary angle on the fatigue crack propagation

The fatigue crack propagation resistance is different between the laser zone and

the arc zone, although they are both composed of lath martensite. This is because the number of the high-angle grain boundaries of the laser zone is different from that of the arc zone. The crack propagation could be effectively prevented by the high-angle grain boundary (>15°) which could also change the crack propagation rate. The larger the number of the high-angle grain boundaries, the stronger the inhibition on the fatigue crack propagation [35-37]. The grain boundary angles of both the laser zone and the arc zone is about 60° [21], which belongs to the category of the high-angle grain boundary. The percentage of the high-angle grain boundary of the laser zone is about 64.2%, while that of the arc zone is 51.8%. The percentage of the high-angle grain boundary of the laser zone increases 24% compared with that of the arc zone. Consequently, the fatigue crack propagation resistance of the laser zone is higher than that of the arc zone. In conclusion, the grain size and the number of the high-angle grain boundary are the main factors that affect the fatigue crack propagation resistance of the laser zone and arc zone.

5. Conclusions

1) This study investigated the fatigue crack propagation of the integral joint welded by DSHW in thick-section high strength steel, as well as that of the laser zone, arc zone and base metal of the joint. Based on the results and analyses, the conclusions are drawn as follows:
2) The double-sided hybrid laser-arc weld is in dumbbell shape. The depth-width ratios of the laser zone and arc zone were 6.3 and 0.5, respectively. The average penetration of the laser zone was about two times that of the arc zone. However,

the average width of the laser zone was only 1/4 that of the arc zone.

3) The base metal consisted of massive polygonal ferrites and small granular carbides, while weld metal were all composed of martensite with a high dislocation density.

4) The average effective grain sizes of the base metal, laser zone and arc zone were 15.8 μm, 4.2 μm and 8.1 μm, respectively. The average effective grain sizes of the laser zone was only 1/2 that of the arc zone due to the faster cooling rate associated with the laser heat resource.

5) The percentages of the grain boundaries with high misorientation angle (>15°) of the base metal, laser zone and arc zone were 50.5%, 64.2% and 51.8%, respectively. The percentage of grain boundaries with high misorientation angle of the laser zone was 24% more than that of the arc zone because the grain size of the laser zone was smaller than that of the arc zone, and the grain boundary angles of both the laser zone and arc zone were about 60°.

6) The fatigue crack propagation resistance of the welded joint was higher than that of the base metal. At the instantaneous fracture stage, the fracture pattern of the base metal and welded joint was similar to typical ductile fracture pattern under static load, i.e. dimples were observed.

7) The fatigue crack propagation resistance of the laser zone was higher than that of the arc zone. When the stress intensity factor range was 80 $MPa \cdot m^{1/2}$, the fatigue crack propagation resistance of the laser zone 17% higher than that of the arc zone, mainly due to the refined grains and the high proportion of the high

misorientation angle grain boundary (>15°).

8) The fatigue crack propagation resistance of thick-section integral welded joint could be enhanced by increasing the laser zone which exhibits deep penetration and narrow width.

Acknowledgments

This research did not receive any specific grant from funding agencies in the public, commercial, or not-for-profit sectors. The authors wish to acknowledge Dr. Jin Peng, Dr. Guolong Ma and Dr. Chuang Cai for useful technical discussions and support during the process of this project.

References

[1] H.J. Kong, C. Xu, C.C. Bu, C. Da, J.H. Luan, Z.B. Jiao, G. Chen, C.T. Liu, Hardening mechanisms and impact toughening of a high-strength steel containing low Ni and Cu additions, Acta Mater. 172 (2019) 150-160.

[2] Z.B. Jiao, J.H. Luan, W. Guo, J.D. Poplawsky, C.T. Liu, Effects of welding and post-weld heat treatments on nanoscale precipitation and mechanical properties of an ultra-high strength steel hardened by NiAl and Cu nanoparticles, Acta Mater. 120 (2016) 216-227.

[3] M. Jiang, W. Tao, Y. Chen, F. Li, Comparison of processing window in full penetration laser welding of thick high-strength steel under atmosphere and sub-atmosphere, Opt. Laser Technol. 109 (2019) 449-455.

[4] N. Matsumoto, Y. Kawahito, K. Nishimoto, S. Katayama, Effects of laser focusing properties on weldability in high-power fiber laser welding of thick high-strength steel plate, J. Laser Appl. 29(1) (2017) 012003.

[5] P.D. Gosavi, K.K. Sarkar, S.K. Khunte, V.R. Pawar, B. Basu, Microstructure and mechanical properties correlation of weld joints of a high strength naval grade steel, in: K.B.S. Rao, R. Sunder, V. Jayaram, S. Gopalakrishnan, K. Gopinath, K. Prasad (Eds.), 2nd International Conference on Structural Integrity and Exhibition 2019, pp. 304-313.

[6] L. Lan, C. Qiu, D. Zhao, X. Gao, L. Du, Analysis of microstructural variation and mechanical behaviors in submerged arc welded joint of high strength low carbon bainitic steel, Mater. Sci. Eng. A 558 (2012) 592-601.

[7] I. Bunaziv, S. Wenner, X. Ren, J. Frostevarg, A.F.H. Kaplan, O.M. Akselsen, Filler metal distribution and processing stability in laser-arc hybrid welding of thick HSLA steel, J. Manuf. Process. 54 (2020) 228-239.

[8] B. Acherjee, Hybrid laser arc welding: State-of-art review, Opt. Laser Technol. 99 (2018) 60-71.

[9] I. Bunaziv, J. Frostevarg, O.M. Akselsen, A.F. Kaplan, Hybrid Welding of 45 mm high strength steel sections, in: M. Kristiansen, S.L. Villumsen (Eds.), 16th Nordic Laser Materials Processing Conference 2017, pp. 11-22.

[10] G. Tang, X. Zhao, R. Li, Y. Liang, Y. Jiang, H. Chen, The effect of arc position on laser-arc hybrid welding of 12-mm-thick high strength bainitic steel, Opt. Laser Technol. 121 (2020) 105780.

[11] L. Li, J. Zheng, C. Wang, Fatigue behavior improvements of laser-induction hybrid welded S690QL steel plates, Opt. Laser Technol. 126 (2020) 106101.

[12] N. Yamaguchi, G. Lemoine, T. Shiozaki, Y. Tamai, Effect of microstructures on notch fatigue properties in ultra-high strength steel sheet welded joint, Int. J. Fatigue 129 (2019) 105233.

[13] A. Trudel, M. Lévesque, M. Brochu, Microstructural effects on the fatigue crack growth resistance of a stainless steel CA6NM weld, Eng. Fract. Mech. 115 (2014) 60-72.

[14] F. Liu, X. Lin, H. Yang, X. Wen, Q. Li, F. Liu, W. Huang, Effect of microstructure on the fatigue crack growth behavior of laser solid formed 300M steel, Mater. Sci. Eng. A 695 (2017) 258-264.

[15] Q. Wang, Z. Yan, X. Liu, Z. Dong, H. Fang, Understanding of fatigue crack growth behavior in welded joint of a new generation Ni-Cr-Mo-V high strength steel, Eng. Fract. Mech. 194 (2018) 224-239.

[16] G. Moeini, A. Ramazani, J. Hildebrand, C. Roessler, C. Koenke, Study of the effect of microstructural variation on the low cycle fatigue behavior of laser welded DP600 steel: Simulation and experimental validation, Mater. Sci. Eng. A 730 (2018) 232-243.

[17] M. Dourado, D. Soares, J. Barbosa, A. Marques Pinho, J. Meireles, P. Branco, C. Ribeiro, C. Rei, A comparative study of fatigue behaviour of MAG and laser welded components using reliability analysis, Mater. Sci. Eng. A 606 (2014) 31-39.

[18] Y. Kim, W. Hwang, Effect of weld seam orientation and welding process on fatigue fracture behaviors of HSLA steel weld joints, Int. J. Fatigue 137 (2020) 105644.

[19] T. Hoshide, T. Yamada, S. Fujimura, T. Hayashi, Short crack growth and life prediction in low-cycle fatigue of smooth specimens, Eng. Fract. Mech. 21(1) (1985) 85-101.

[20] M. Marx, W. Schaef, M.T. Welsch, The microstructure as crack initiation point and barrier against fatigue damaging, Int. J. Fatigue 41 (2012) 57-63.

[21] Y. Chen, J. Feng, L. Li, S. Chang, G. Ma, Microstructure and mechanical properties of a thick-section high-strength steel welded joint by novel

double-sided hybrid fibre laser-arc welding, Mater. Sci. Eng. A 582 (2013) 284-293.

[22] J. Feng, L. Li, Y. Chen, Morphology and crystallography of lath martensite in weld metal of high strength steel by double sided laser welding, Mater. Lett. 261 (2020) 127129.

[23] P. Paris, F. Erdogan, A critical analysis of crack propagation laws, J. Basic Eng. 85 (1963) 528–533.

[24] A. Mesgarnejad, A. Imanian, A. Karma, Phase-field models for fatigue crack growth, Theor. Appl. Fract. Mech. 103 (2019) 102282.

[25] H. Remes, P. Gallo, J. Jelovica, J. Romanoff, P. Lehto, Fatigue strength modelling of high-performing welded joints, Int. J. Fatigue 135 (2020) 105555.

[26] S. Sajith, S.S. Shukla, K.S.R.K. Murthy, P.S. Robi, Mixed mode fatigue crack growth studies in AISI 316 stainless steel, Eur. J. Mech. A-Solids 80 (2020) 103898.

[27] J. Ni, Z. Li, J. Huang, Y. Wu, Strengthening behavior analysis of weld metal of laser hybrid welding for microalloyed steel, Mater. Des. 31(10) (2010) 4876-4880.

[28] X. Cao, P. Wanjara, J. Huang, C. Munro, A. Nolting, Hybrid fiber laser-arc welding of thick section high strength low alloy steel, Mater. Des. 32(6) (2011) 3399-3413.

[29] M. Velu, A short review on fracture and fatigue crack growth in welded joints, Mater. Today: Proc. 5(5) (2018) 11364-11370.

[30] X. Li, S. Hu, J. Xiao, L. Ji, Effects of the heterogeneity in the electron beam welded joint on fatigue crack growth in Ti–6Al–4V alloy, Mater. Sci. Eng. A 529 (2011) 170-176.

[31] P.J.E. Forsyth, D.A. Ryder, Fatigue fracture: some results derived from the microscopic examination of crack surfaces, Aircr. Eng. Aerosp. Technol. 32(4) (1960) 96-99.

[32] C.F. Shih, R.J. Asaro, Elastic-plastic analysis of cracks on bimaterial interfaces: part I-small scale yielding, J. Appl. Mech. 55(2) (1988) 299-316.

[33] S. Ueki, T. Matsumura, Y. Mine, S. Morito, K. Takashima, Microstructural fatigue crack growth in single-packet structures of ultra-low carbon steel lath martensite, Scr. Mater. 173 (2019) 80-85.

[34] S. Ueki, Y. Mine, K. Takashima, Microstructure-sensitive fatigue crack growth in lath martensite of low carbon steel, Mater. Sci. Eng. A 773 (2020) 138830.

[35] E.Bouyne, H.M. Flower, T.C. Lindley, A. Pineau, Use of EBSD technique to examine microstructure and cracking in a bainitic steel, Scr. Mater. 39(3) (1998) 295-300.

[36] A. Lambert, X. Garat, T. Sturel, A.F. Gourgues, A. Gingell, Application of acoustic emission to the study of cleavage fracture mechanism in a HSLA steel, Scr. Mater. 43 (2000) 161-166.

[37] A.L. Perlade, A.F. Gourgues, J. Besson, T. Sturel, A. Pineau, Mechanisms and modeling of cleavage fracture in simulated heat-affected zone microstructures of a high-strength low alloy steel, Metall. Mater. Trans. A 35(13) (2004) 1039-1053.

2020-10-13

Inhomogeneous microstructure and fatigue crack propagation of thick-section high strength steel joint welded using double-sided hybrid fiber laser-arc welding

Feng, Jiecai

Elsevier

Feng J, Li L, Chen Y, et al., (2021) Inhomogeneous microstructure and fatigue crack propagation of thick-section high strength steel joint welded using double-sided hybrid fiber laser-arc welding. Optics and Laser Technology, Volume 134, February 2021, Article number 106668 https://doi.org/10.1016/j.optlastec.2020.106668